Theor Appl Climatol
DOI 10.1007/s00704-009-0139-4

ORIGINAL PAPER

Climate version of the ETA regional forecast model

Evaluating the consistency between the ETA model and HadAM3P global model

I. A. Pisnichenko · T. A. Tarasova

Received: 18 August 2008 / Accepted: 14 April 2009

Abstract A new version of ETA WS (workstation) forecast model destined for long-term climate change simulation (ETA CCS) was designed. Numerous modifications and corrections have been made in the original code of the ETA WS forecast model. As a first step in the ETA CCS validation program, we have integrated the model over South America with a horizontal resolution of 40 km for the period 1960–1990. We forced it at its lateral boundaries by the outputs of HadAM3P, which provides a simulation of modern climate with a resolution of about 150 km. The climate ETA model was run on the supercomputer SX-6. Here, we present and compare the output fields of the ETA model and HadAM3P and analyze the geopotential, temperature, and wind fields of both models. For evaluating the similarities of the model outputs, we used a Fourier analysis of time series, the consistency index from linear regression coefficients, the time mean and space mean models' arithmetic difference and root mean square difference. The results of the study demonstrate that there are no significant differences in behavior and spatial arrangement of large-scale structures of the two models. In addition, the regional model characteristics do not have major positive or negative trends during the integration in relation to the global model. Our analysis shows that the descriptions of large-scale climate structures by these two models are consistent. This means that the ETA CCS model can be used for downscaling HadAM3P output fields. Our proposed technique can be used to evaluate the consistency of any regional model and its driving global model.

I. A. Pisnichenko (✉)
Center of Weather and Climate Studies/National Institute of Space Research (CPTEC/INPE),
Rod. Pres. Dutra, km. 39,
Cachoeira Paulista, SP, Brazil
e-mail: igorap@cybergal.com

T. A. Tarasova
Center of Earth System Science/National Institute of Space Research (CCST/INPE),
Rod. Pres. Dutra, km. 39,
Cachoeira Paulista, SP, Brazil

T. A. Tarasova
Institute of Atmospheric Physics, Russian Academy of Sciences,
Moscow, Russia

1 Introduction

Running a regional climate model (RCM) with a horizontal resolution of a few tens of kilometers with boundary conditions from AOGCM for 10–30 years for the present climate and future projections can provide additional information about regional-scale climate and climate-change effects (e.g., Dickinson et al. 1989; Giorgi and Bates 1989). Such downscaling studies related to climate change have been done for various parts of Europe, North America, Australia, and Africa (see, e.g., the references cited by Jones et al. 1997; Laprise et al. 2003; Giorgi et al. 2004; Duffy et al. 2006). Some large projects, such as PRUDENCE (Christensen et al. 2007) and NARCCAP (http://www.narccap.ucar.edu), launched to investigate uncertainties in the RCM climate-change simulations over Europe and North America, are currently underway. Multiple regional climate model ensembles are used in these studies to minimize uncertainties. The project "Climate change scenarios using PRECIS" (Jones et al. 2004) was launched by the Hadley Center for Climate Prediction and Research to develop a user-friendly RCM that can be easily run on a personal computer for any area of the globe. The data of the atmospheric global model HadAM3P were provided by the Hadley Center to CPTEC/INPE to be used as boundary conditions over South America.

In order to be considered a valid tool for dynamically downscaling low-resolution GCM fields, a regional climate model must satisfy certain requirements (e.g., Wang et al. 2004; Castro et al. 2005; Laprise 2006). First, it must show that the RCM can more or less plausibly reproduce mean values and second moments of the large-scale fields of GCM, which provides the data used as driving boundary conditions. This is a necessary condition indicating that nonlinear interactions of small-scale components do not strongly divert the system from the background state. It also guarantees that boundary conditions will not transform into peculiarities. This is an issue in evaluating the consistency between RCM and GCM fields. Second, for successful downscaling, the RCM must be able to add small-scale features that are absent in the GCM driving fields; these features must agree with observations and high-resolution GCM fields. Laprise et al. (2008) provide a summary of studies related to this. As it was annotated in this paper, the consensus on the first point is not yet reached within the RCM community. It is not quite clear from the analysis of RCM runs if the large scales of GCM are unaffected, improved, or degraded by RCMs. We also note that large-scale fields of RCM and GCM are usually compared for surface temperature and precipitation (e.g., Hudson and Jones 2002; Seth et al. 2007). Another type of comparison is presented by Castro et al. (2005) for the 1-month simulation of the Regional Atmospheric Modeling System (RAMS; Pielke et al. 1992) with the boundary conditions of the reanalysis. They did a spectral analysis of the column average total kinetic energy and the column integrated moisture flux convergence and concluded that RAMS does not improve the large-scale components of these characteristics in comparison with the reanalysis.

Here, we propose to use the regional climate model prepared from the NCEP ETA regional forecast model (Black 1994) in climate downscaling research. Until now, long integrations with the ETA model have been limited to continuous integrations for 3 or 5 months (Chou et al. 2000; Tarasova et al. 2006; Fernandez et al. 2006) because of limitations in the codes of the ETA model that were developed for weather forecast and studies. The climate version of the ETA model that permits integrations for periods of any duration have been developed at the Brazilian Instituto Nacional de Pesquisas Espaciais/Centro de Previsao de Tempo e Estudos Cimaticos (INPE/CPTEC) (Pisnichenko et al. 2006).

In the present work, we show the first results related to developing a climate version of the ETA model for climate downscaling over South America. We investigate the consistency of the large-scale output fields of the ETA model and HadAM3P. For this, we analyzed the geopotential, temperature, and wind fields at various levels using Fourier analysis of time series, the consistency index derived from linear regression coefficients, the time mean and space mean models' arithmetic difference (MAD), the root mean square difference (RMSD), and other characteristics. A short description of the ETA model and of implemented modifications is given in Section 2, where the model integration procedure is also described. The newly developed version of the ETA model is hereafter termed the INPE ETA for Climate Change Simulations (INPE ETA CCS). Section 3 presents the results of integrations with the INPE ETA CCS model over South America driven by boundary conditions from the HadAM3P for the period 1961–1991. We compare the ETA model output fields with those from HadAM3P so as to prove consistency between the two models. Section 4 provides a summary of the results and conclusions.

2 Model and experimental design

For this work, aimed to prepare the ETA model version for climate change simulations, we initially adopted the workstation (WS) ETA modeling package (2003 version) developed at the Science Operations Officer/Science and Training Resource Center (SOO/STRC), which is freely available at http://strc.comet.ucar. The SOO/STRC WS ETA is nearly identical to the WS ETA model and operational 2003 ETA Model, both of which were developed at NCEP. Only the run-time scripts and model file organization were changed, and the convection cumulus scheme of Kain and Fritsch (1993) was added. The longest continuous integration with this model is 1 month due to restrictions resulting from its weather forecast destination.

2.1 Short description of the NCEP ETA model

A full description of the NCEP ETA regional forecasting model is given by Mesinger et al. (1988), Janjic (1994), and Black (1994). In brief, the horizontal field structure is described on a semi-staggered E grid. The ETA vertical coordinate ($\eta = [(p - p_{\mathrm{T}})/(p_{\mathrm{sfc}} - p_{\mathrm{T}})]/\eta_{\mathrm{srf}}$, where p is a pressure, p_{T} and p_{sfc} are the pressures at the top and bottom of the model boundary, respectively, and η_{srf} is a reference η) is used to reduce numerical errors over mountains in computing the pressure gradient force. The planetary boundary layer processes are described by the Mellor-Yamada level 2.5 model (Mellor and Yamada 1974). The convective precipitation scheme is from Betts and Miller (1986) as modified by Janjic(1994). The shortwave and longwave radiation codes follow the parameterizations of Lacis and Hansen (1974) and Fels and Schwartzkopf (1975), respectively. The land-surface scheme is from Chen et al. (1997). The grid-scale cloud cover fraction is parameterized as a function of relative humidity and the cloud water (ice) mixing ratio (Xu and Randall 1996; Hong et al. 1998). Convective cloud cover fraction is parameterized as a function of precipitation rate (Slingo 1987).

2.2 Modifications in the SOO/STRC WS ETA model

We installed the SOO/STRC WS ETA model at the supercomputer NEC SX6 at CPTEC. In order to perform long-term climate integrations, we made multiple changes and corrections in the scripts and source codes of the original model and wrote additional subroutines.

As mentioned above, the ETA model was forced at its lateral and bottom boundaries by the output of the HadAM3P model. The HadAM3P output data represent horizontal wind, potential temperature, specific humidity, and earth surface pressure, which are given on the horizontal Arakawa B-grid and at the 19 sigma-hybrid levels. These data are written in the PP-format. To use them for the ETA model boundary conditions, these data must be transformed into horizontal wind, geopotential, mixture ratio, and earth surface pressure given on a regular latitude–longitude grid at the standard p surface levels. For this, we modified some of the pre-processing ETA model programs and wrote a new program that converts the HadAM3P output data to a form acceptable by the ETA model.

Other modifications made in the ETA model are briefly described below. The SST update programs used to accept the SST and SICE data generated by the coupling model HadCM3 every 15 days were rewritten. The programs for the Sun's elevation angle and the calendar were modified in order to be able to integrate the ETA model for the artificial year of 360 days that is used by HadAM3P. New restart programs were developed, which allow us to continue the model integration from any moment in time by using the model output binary files; these can be used in the multiprocessing integration. This restart possibility is very useful for a long-term climate integration because of the large size of the boundary condition file needed for continuous integrations. Another reason we used a restart option is the large size of the output binary files, which, after post-processing, can be written in the more economic GRIB format. All shortcomings that restrict a period of model integration were corrected, including those in the post-processing subroutines.

The additional solar radiation scheme (CLIRAD-SW-M) developed by Chou and Suarez (1999) and modified by Tarasova and Fomin (2000) was implemented in the model. The results of the month integration with this scheme were analyzed by Tarasova et al. (2006). The additional thermal radiation scheme of Chou et al. (2001) was also implemented. This allows us to run the model with an increasing concentration of CO_2 and other trace gases needed for future climate simulation experiments. All of these corrections, modifications, and implementations were made taking into account that the model can be run on a Linux cluster or other multiprocessor computer.

2.3 Integration with the INPE ETA CCS model

The first step in evaluating dynamical downscaling results is investigating the consistency between regional model outputs and GCM data used for RCM boundary conditions. That is, we must show that our RCM does not significantly diverge from GCM in reproducing time mean large-scale circulation patterns. We note that the results of regional modeling, as they are the solution of a Cauchy–Dirichlet problem, can be very sensitive to errors in lateral boundary conditions (Pisnitchenko et al. 2008). These errors are always present because we use a linear interpolation of time-dependent boundary conditions (data every 6 h) into intermediate time steps. In other words, we want to be sure that our model is not crucially influenced by boundary condition errors and that most stable and pronounced disturbances present in the GCM are reproduced by our RCM. We also expect that a low-frequency oscillation of the atmosphere should be simulated by both models in a similar manner. These are necessary conditions to avoid erroneously generating small and middle-scale disturbances resulting from nonlinear interactions in RCM. The consistency of the outputs of the ETA CCS RCM and driving GCM must also be verified due to differences of the physical parameterization packages of the two models.

To accomplish this, we analyzed the results of the ETA CCS model integration for the period 1960–1990 over South America. These data are part of the results of current and future climate downscaling experiments covering the periods 1960–1990 and 2071–2100, respectively. Our group is working on a detailed analysis of all the results of these experiments, which we will present in further publications.

The ETA CCS model in our experiments was forced at its lateral and bottom boundaries by the output of HadAM3P, which was run using SST, SICE (sea ice), greenhouse gases, and aerosol concentration as drivers external obtained from the coupling model HadCM3. The data for lateral boundary conditions for the ETA CCS model were provided every 6 h, and SST and SICE data were provided every 15 days. Linear interpolation for the lateral boundaries, SST, and SICE was used between these periods. For the initial conditions of soil moisture and soil temperature, the climate mean values were used. The spin-up period of soil moisture and temperature was accepted as equal to 1 year. Hence, the first year of integration was not used in the analysis.

The area of integration was centered at 58.5° W longitude and 22.0° S latitude and covers the territory of the South American continent with adjacent oceans (55° S–16° N, 89° W–29° W). The model was integrated on the 211×115 horizontal grid with a grid spacing of 37 km. In the vertical, the 38 ETA coordinate layers were used. For the modern climate integration in the consistency experiment, we chose the Betts–Miller cumulus convection parameterization scheme and the ETA model original shortwave and longwave radiation schemes.

3 Analysis of the integration results

In order to show consistency between the ETA CCS and HadAM3P models, we compared the geopotential height, temperature and kinetic energy fields on the earth surface and at the various p-levels (1,000, 700, 500 hPa) from these two data sources. A more detailed comparison was made for the five regions shown in Fig. 1: Amazonia (12.5° S–5° N, 75° W–48.75° W); Nordeste (northeast of Brazil) (15° S–2.5° S, 45° W–33.75° W); Southern Brazil (32.5° S–22.5° S, 60° W–48.75° W); Minas (22.5° S–15° S, 48.75° W–41.25° W); and Pantanal (17.5° S–12.5° S, 60° W–52.5° W). The time-averaged fields and time series of space-averaged meteorological variables were analyzed.

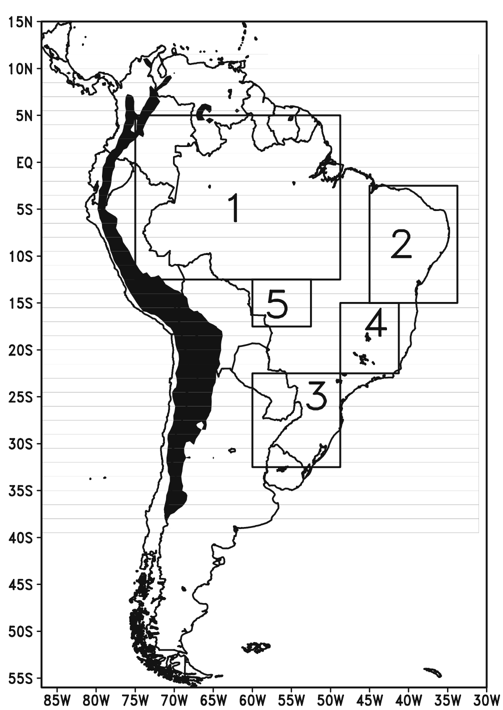

Fig. 1 The regions over South America selected for the analysis: *1* Amazonia, *2* Nordeste, *3* Sul Brasil, *4* Minas, *5* Pantanal

3.1 Analysis methods

To evaluate the consistency between the outputs of the ETA CCS regional climate model (hereafter RCM) and the HadAM3P global climate model (hereafter GCM), we used various measures. First, we assessed the climatological means and time-averaged difference between the models, which allowed us to identify systematic differences between the models. We then analyzed various characteristics (root mean square difference, coefficients of linear regression, consistency index, spectra of time series), which allowed us to show in detail a distinction between the GCM and RCM simulated fields. Since this work is dedicated to investigating the RCM abilities to reproduce mean fields of driving GCM and some of their statistical moments, we scaled the regional model fields to the global model grid. For this, we removed the small-scale component from the regional model fields by applying a smoothing filter. This filter is the two-dimensional version of the weighted moving average, where weights depend linearly on the distance between the grid points of the global model and the grid points of the regional model (at which the data used in the smoothing procedure are located). The weight increases when the distance decreases. This smoothing procedure can be written as:

$$\Phi(x_i, y_j) = \sum_{r_{i,j;k} < r_0} \phi(\widehat{x}_k, \widehat{y}_k) p_k, \tag{1}$$

where $\Phi(x_i, y_j)$ is a smoothed value of the regional model field at a global grid point, r_0 is the radius of influence that defines the circle inside which the RCM field data are used for calculating the average, $r_{i,j;k}$ is the distance from a (x_i, y_j) point of the GCM grid to the k-th RCM grid point $(\widehat{x}_k, \widehat{y}_k)$, $\varphi(\widehat{x}_k, \widehat{y}_k)$ are the field values at the k-th RCM grid point inside the circle defined by the radius of influence, and p_k is a weight for the k-th RCM grid point, which is calculated as

$$p_k = \left(1 - \frac{r_{i,j;k}}{r_0}\right) / \left(\sum_{r_{i,j;k} < r_0} 1 - \frac{1}{r_0} \sum_{r_{i,j;k} < r_0} r_{i,j;k}\right). \tag{2}$$

In this formula, the numerator decreases with increasing $r_{i,j;k}$ and becomes equal to zero when $r_{i,j;k}$ is equal to or larger than r_0. The denominator is defined from a normalization condition; i.e., a sum of all p_k weights inside the circle must be equal to 1.

In order to compare the models in general, we analyzed how well they reproduce the time-averaged fields of meteorological variables and the standard deviations fields of these variables. For a more detailed assessment of the consistency between the RCM and GCM fields, we calculated the models' arithmetic difference and coefficients of linear regression using the time-series of meteorological variables at each common grid point of the RCM and GCM models. The fields of these characteristics provide useful information about the degree of consistency of the models results.

For a quantitative and direct description of the consistency between the RCM and GCM output fields, we propose a new characteristic, which we term the consistency index (CI). This characteristic represents an integral variant of the Taylor diagram (Taylor 2001). It is a simple function that depends on the coefficients of linear regression of GCM output on RCM output, standard deviations and mean values of compared series. This function expresses the resemblance of one field to another.

We found that this characteristic was useful as it can describe the similarity of two fields by a single number when the space patterns are analyzed. The use of a unique number for describing the resemblance of two random series is of particular interest when the consistency of the time evolution of space patterns is analyzed. In this case, we can analyze the time series of compared fields at every grid point and describe the resemblance of the time evolution of the fields by a single field (the consistency index number at each grid point).

We define the numeric value of the CI as:

$$CI = \begin{cases} \left(1 - \frac{\Delta S_{\mathrm{d}}}{\Delta S_{\mathrm{n}}}\right) \frac{\sigma_{\mathrm{G}}}{\sigma_{\mathrm{R}}} \text{ for } \frac{\sigma_G}{\sigma_R} \leq 1, \\ \left(1 - \frac{\Delta S_{\mathrm{d}}}{\Delta S_{\mathrm{n}}}\right) \frac{\sigma_{\mathrm{R}}}{\sigma_{\mathrm{G}}} \text{ for } \frac{\sigma_G}{\sigma_R} > 1. \end{cases} \quad (3)$$

Here, σ_{G} and σ_{R} are the sample standard deviations of an investigated meteorological parameter of a global model series and a regional model series, respectively. The ΔS_{d} is the area of figure *ABOCD* (see Fig. 2), which is formed by two straight lines of linear regression and two vertical lines that intersect them. The straight line *r* is a linear regression line of the GCM series on the RCM series, while the straight line *i* is an ideal regression line for the identical GCM and RCM series with regression coefficients $a0=0$ and $a1=1$. The two vertical lines that intersect these regression lines have the coordinates $x_{\mathrm{R}}=a-s$ and $x_{\mathrm{R}}=a+s$. *a* is the mean value of the investigated meteorological parameter of the RCM series normalized on $s_0=1.44\sigma_{\mathrm{R}}$, and *s* is the nondimensional value of s_0. The interval $(a-s, a+s)$ contains 85% of the members of the RCM series (under the assumption that the series obeys a Gaussian distribution). ΔS_{n} is the area of triangle *BCE*. The area of the shaded figure *ABOCD* statistically describes the degree of resemblance of the GCM and RCM series: a smaller area corresponds to a closer resemblance. The area of triangle *BCE* is equal to 2 in nondimensional coordinates and describes the case when the RCM and GCM series are noncorrelated and the mean value of the GCM series is equal to $a-s$ (or $a+s$). The multiplier $\frac{\sigma_G}{\sigma_R}$ (or $\frac{\sigma_R}{\sigma_G}$) approximately describes the ratio of transient-eddy amplitudes reproduced by the models. Ideally, these amplitudes are very close. The magnitude of the CI is close to 1 if the GCM and RCM series statistically resemble one another and is equal or less than zero when there is no similarity. When *ABOCD* is larger than *BCE*, the CI magnitude is less than zero, which means that the resemblance of the series is worse than for noncorrelated series with the mean value of the GCM series smaller (or larger) than $a+s$ $(a-s)$.

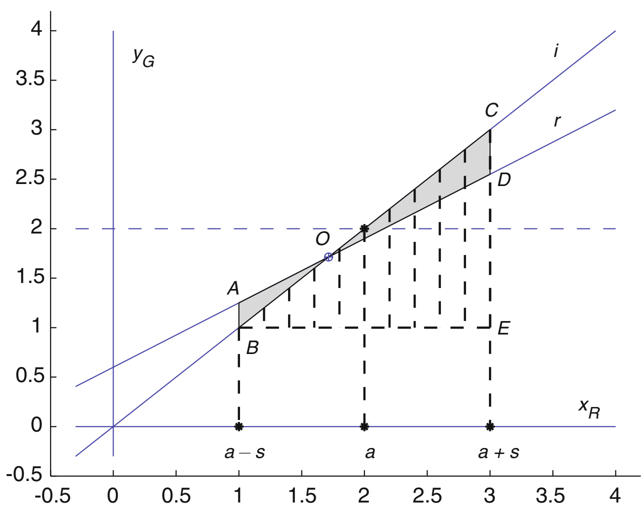

Fig. 2 Definition of consistency index by using the coefficients of linear regression of HadAM3P field on ETA CCS model field

Since we had to process a very large number of data, we used recurrence formulas to calculate averages, sample standard deviations, and coefficients of linear regression for various GCM and RCM series and wrote these characteristics to the model output every 24 h. These characteristics for any time period can be recalculated from these running statistics. The recurrence formulas and formulas that were used for recalculation are presented in Appendix 1.

3.2 Assessing RCM and GCM consistency

We first present the geopotential height, temperature, and kinetic energy fields averaged over the period of integration from 1961 to 1990. Figure 3 shows these fields at the level of 1,000 hPa from the RCM and GCM simulations. The ETA model can reproduce the main patterns of the HadAM3P fields. In the geopotential height field, RCM reproduces the minimum over the northern part of the continent and the maxima over the subtropical Atlantic and Pacific. In the temperature fields, the RCM reproduces the maximum over the central part of the continent and the strong north–south gradient south of 30º S. The magnitude of the temperature is higher everywhere in the ETA model than in the GCM, especially over the central part of the continent; this is probably related to the lack of convective cloudiness in this region (Tarasova et al. 2006). Notice, that the main part of the domain is located in Tropics and sub-

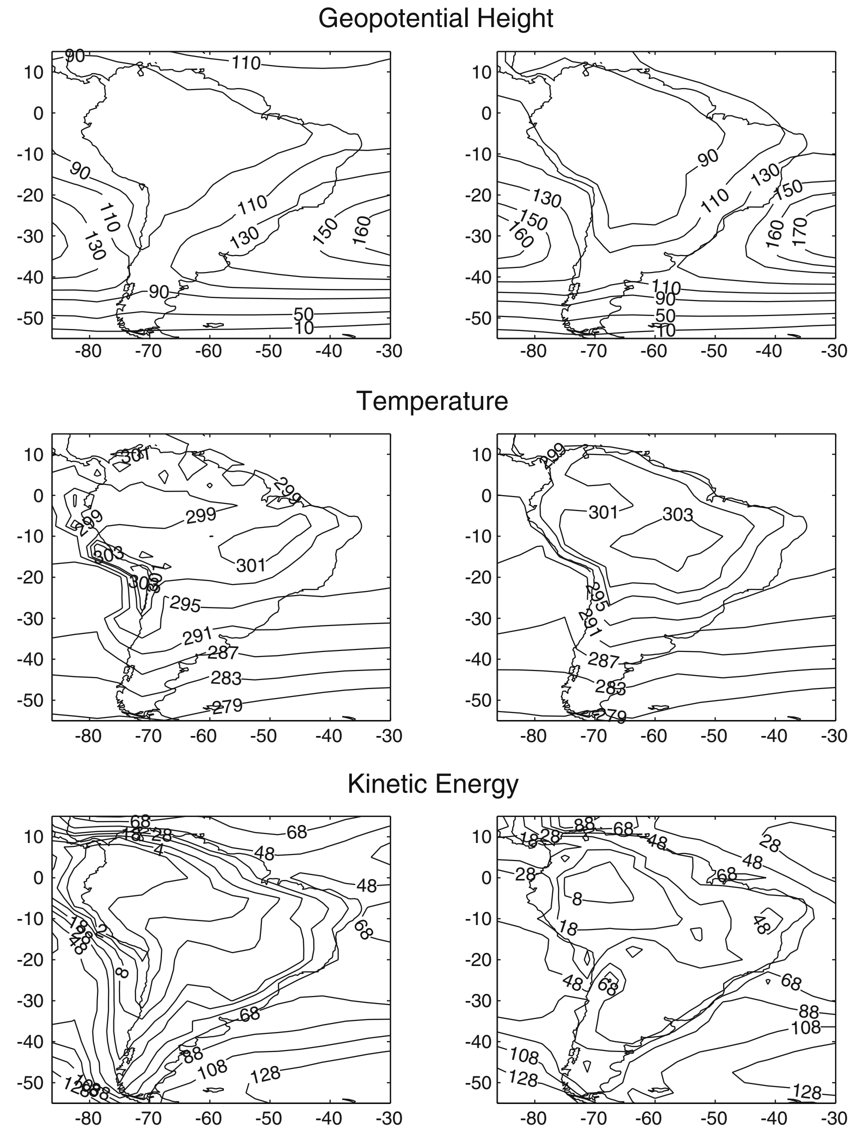

Fig. 3 Mean (1961–1990) fields of geopotential height (*m*), temperature (K), and kinetic energy ($m^2\ s^{-2}$) at 1,000 hPa, provided by HadAM3P (*left*) and ETA CCS model (*right*) simulations

Tropics where convective processes simulated by RCM strongly affect the formation of cloudiness and, hence, the temperature fields particularly near the surface. The fields of RCM and GCM in the inner region can differ also for the reason of different physical parameterization and boundary conditions errors arising from the time interpolation and the procedure of space interpolation (when drawing isolines). We have to notice that the difference on the eastern boundary is small. For example for the temperature, maximum can reach 1.5 C. But on the western boundary the errors are larger because of the interpolation errors appearing from the large difference of the RCM and GCM fields over Andes.

When we write that the RCM can reproduce the main GCM patterns it means that topology of isolines of variables considered here, specifically the position of max and min of gradients, for GCM and large-scale disturbances of RCM are in general correspondence. Details and values of variables can be slightly different.

RCM and GCM consistently reproduce a west–north to east–south gradient in the kinetic energy field. The numeric values of kinetic energy, however, differ slightly over most of the continent and are greater for the RCM. This is related to the different physical parameterization packages in these models. The same RCM and GCM fields at the higher level of 700 hPa bear a closer spatial and quantitative resemblance (not shown). We note that the fields similarities at 500 hPa are higher than that at 700 hPa (not shown). This is a consequence of the diminishing impact of surface–atmosphere interaction on the higher-level atmospheric circulation. We also compared the same RCM and GCM fields averaged over January and July (not shown). The agreement between the fields is better in July (austral winter, when the impact of dynamics on circulation is larger than the impact of radiation-convective physics) than in January (austral summer, when the dynamical processes are weaker).

The fields of time standard deviation (SD) of meteorological variables provide additional information about the amplitudes of their temporal fluctuations. Figure 4 presents the RCM and GCM SD fields of geopotential height, temperature, and kinetic energy at the 1,000 hPa level averaged over the period of integration. There is a high degree of consistency between the RCM and GCM standard deviation fields (better than for the mean fields). The standard deviation fields also bear a closer resemblance for geopotential height and temperature than for kinetic energy. With increasing altitude, the difference between the RCM and GCM SD fields is diminished for all variables (not shown).

The quantitative distinction between the two fields is usually described by the field of the models' arithmetic difference (MAD), which is the difference between the fields values at each grid point. The left column of Fig. 5 shows the MAD between the RCM and GCM geopotential height, temperature, and kinetic energy fields at 1,000 hPa averaged over the period of integration. The largest values of the MAD fields are over the tropical and subtropical parts of South America. The significant values of the MAD over the Andes are related to errors of interpolation from the sigma-hybrid surfaces to the pressure surfaces located below the Earth's surface in the global model. The values of the MAD decrease for all fields with increasing altitude (700, 500 hPa). The MAD of these variables (geopotential height, temperature, and kinetic energy) averaged over July (January) is smaller (larger) than that averaged over the entire period of integration.

The right column of Fig. 5 presents the consistency index (CI) fields for geopotential height, temperature, and

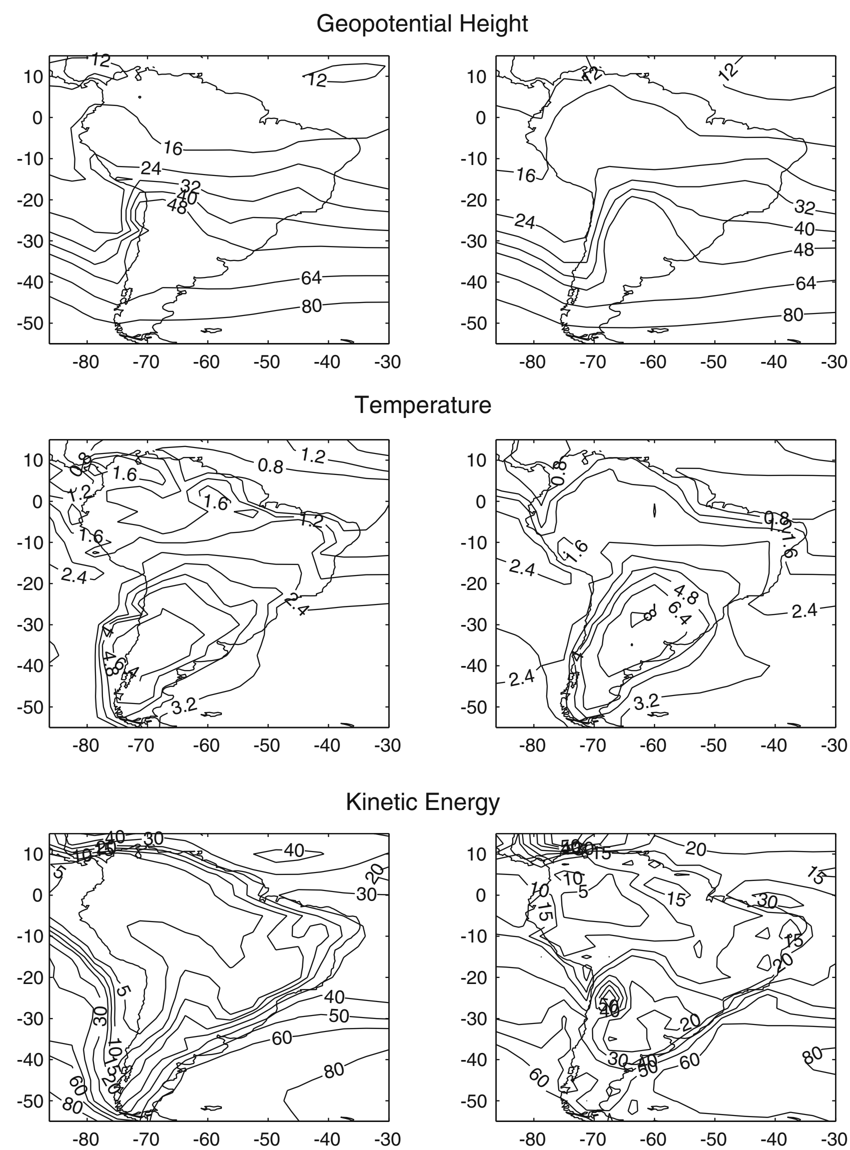

Fig. 4 Mean (1961–1990) SD fields of geopotential height (m), temperature (K), and kinetic energy ($m^2\ s^{-2}$) at 1,000 hPa, provided by HadAM3P (*left*) and ETA CCS model (*right*) simulations

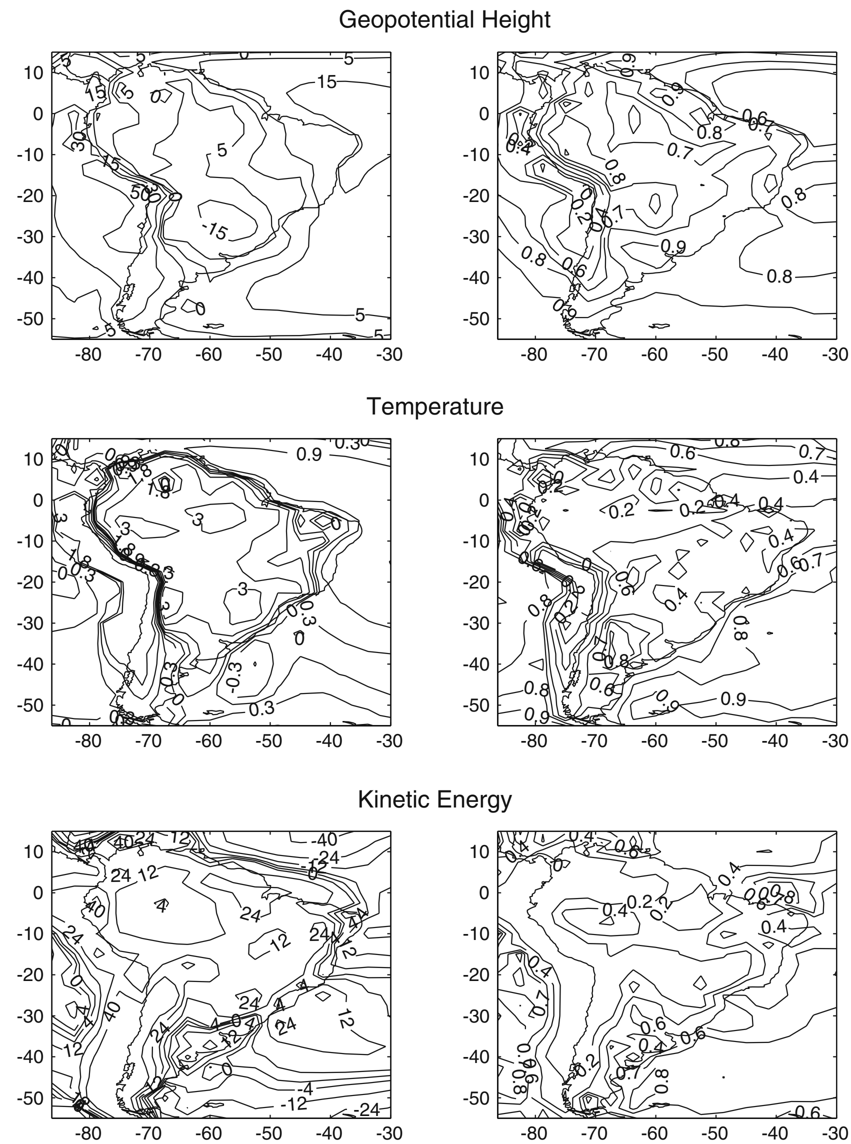

Fig. 5 Mean (1961–1990) fields of MAD (*left*), calculated for HadAM3P and ETA CCS model fields of geopotential height (m), temperature (°K), and kinetic energy ($m^2\ s^{-2}$) at 1,000 hPa, and consistency index between HadAM3P and ETA CCS model (*right*), calculated for the same fields

kinetic energy at the level of 1,000 hPa. A CI close to 1 indicates a good resemblance between the RCM and GCM time evolution of the variables. The CI fields resemble the fields of the MAD in terms of spatial distribution. The large absolute values of the MAD are correlated with small values of CI. Using a nondimensional CI allows us to quantitatively compare the similarity of the fields of different meteorological variables. Thus, the CI fields in Fig. 5 show that the consistency of the fields of geopotential height is higher than that of the temperature fields, and the consistency of the kinetic energy field is lower than that of both geopotential height and temperature.

In order to compare the model outputs, we also analyzed temporal variations of geopotential height, temperature, and kinetic energy values at 1,000, 700, and 500 hPa levels, averaged over the whole integration domain and over the regions shown in Fig. 1. Figure 6 presents the monthly mean models' arithmetic differences and root mean square differences (RMSD) between the GCM and RCM time series for these variables averaged over the whole integration domain. For each variable, the upper figure represents the MAD and the lower figure shows the RMSD. It is clearly seen that the magnitude of the mean MAD is not high: it is about 6 m in geopotential height, less than 0.1 K in temperature, and about 10 $m^2\ s^{-2}$ in kinetic energy at 1,000 hPa. The values of the mean RMSD at 1,000 hPa are also not high. Its magnitude is about 24 m in geopotential height, 3.4 K in temperature, and 39 $m^2\ s^{-2}$ in kinetic energy. Low values of the RMSD prove that the current absolute values of the MAD are not high for each moment of integration. Figure 6 also shows that there is no permanent systematic drift of the MAD and RMSD during the integration, which proves both RCM integration stability and the similar response of RCM and GCM to

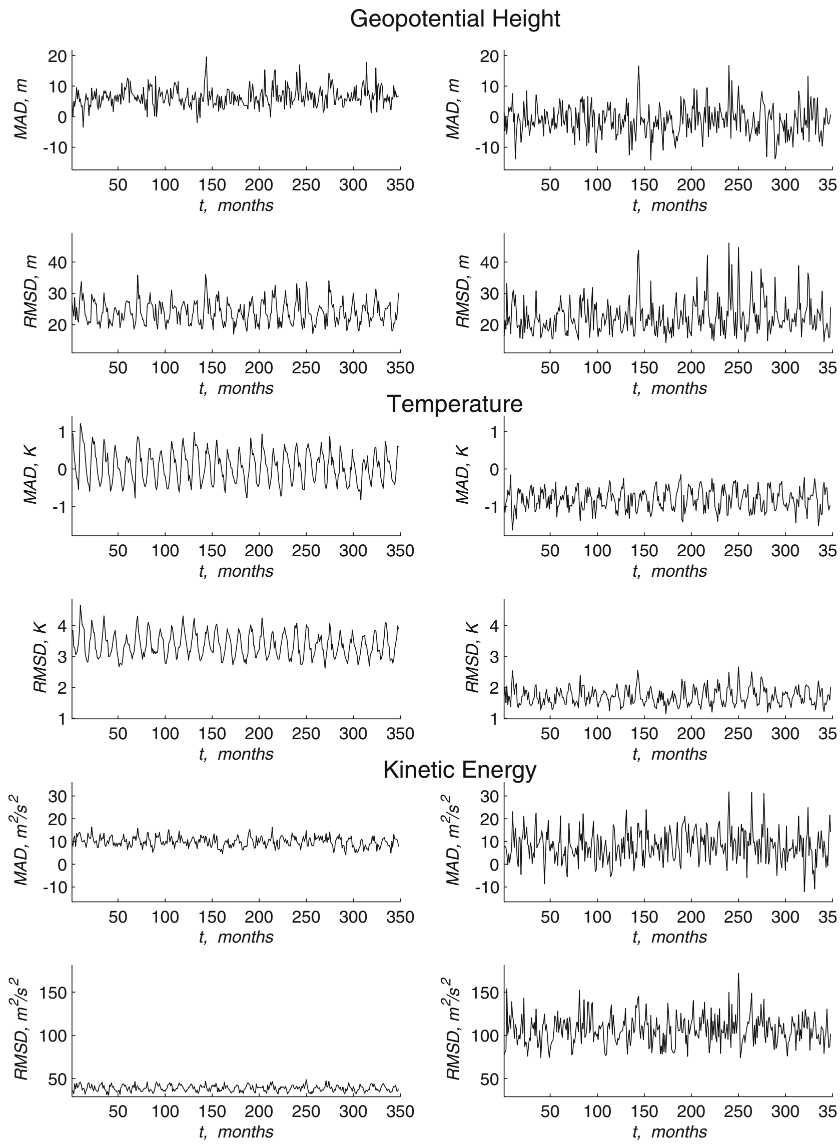

Fig. 6 Time series of mean (over the integration domain) MAD and RMSD, calculated for HadAM3P and ETA CCS model fields of geopotential height (m), temperature (K), and kinetic energy (m^2 s^{-2}) at 1,000 hPa (*left*) and 500 hPa (*right*)

the long-term forcing component. The magnitude of the temporal correlation coefficient between the time series of the RCM and GCM space-averaged fields is about 0.95–0.98. This means that RCM principally follows the GCM boundary drivers. At the level of 700 (not shown) and 500 hPa, the absolute values of both the MAD and RMSD are lower than at 1,000 hPa for temperature. For the geopotential height and kinetic energy, which largely increase with altitude, it is necessary to compare normalized mean values for the MAD and RMSD. The relative MAD and RMSD for the geopotential height and kinetic energy also decrease with altitude.

We also analyzed the same time series for the following regions: Amazonia, Nordeste, Southern Brazil, Minas, and Pantanal, shown in Fig. 1. The correlation coefficients between the RCM and GCM time series as well as the mean MAD and RMSD at 1,000 and 500 hPa are shown in Table 1 for the whole domain and the five regions. These coefficients vary slightly from region to region. We note one case of low correlation between the kinetic energy time series at 1,000 hPa in Amazonia related to a low magnitude of wind at the surface level in GCM. Figure 7 shows the time evolution of the annual mean MAD in the geopotential height, temperature and kinetic energy fields at 1,000 hPa for the above-mentioned regions. The magnitude of the MAD for different regions varies from −17 to +10 m for geopotential height, from −0.3 K to +4.0 K for temperature, and from 5 to 20 m^2 s^{-2} for kinetic energy. The amplitude of interannual variations of these meteorological variables differs by region. There is no significant trend or strong fluctuations of the MAD for any region, and there is no significant mutual correlation between the MAD obtained for the various regions. This indicates that local physical processes and small scales in RCM are, in general,

Table 1 Mean correlation coefficient (r), mean MAD, and mean RMSD between the regional and global models time series of geopotential height (G), temperature (T), and kinetic energy (KE) at 1,000 and 500 hPa, averaged over the integration domain (D) and over the five regions shown in Fig. 1

Region	G			T			KE		
	r	MAD	RMSD	r	MAD	RMSD	r	MAD	RMSD
Pressure level of 1,000 hPa									
D	0.98	6	24	0.98	0.1	3.4	0.95	10	39
1	0.95	−3	9	0.78	2.5	3.0	0.51	13	17
2	0.97	9	13	0.92	−0.2	1.7	0.9	8	23
3	0.97	−15	25	0.96	2.5	4.2	0.83	12	27
4	0.95	−2	17	0.72	1.7	3.0	0.69	14	20
5	0.97	−6	14	0.64	2.4	3.5	0.79	20	22
Pressure level of 500 hPa									
D	0.97	−1	23	0.99	−0.8	1.7	0.98	8	11
1	0.97	−2	6	0.81	−1.0	1.4	0.81	13	42
2	0.94	−1	8	0.81	−0.9	1.5	0.61	12	40
3	0.89	3	26	0.97	−1.0	1.8	0.93	7	111
4	0.74	2	16	0.88	−1.1	1.6	0.86	9	55
5	0.77	−1	10	0.79	−1.6	1.8	0.84	11	36

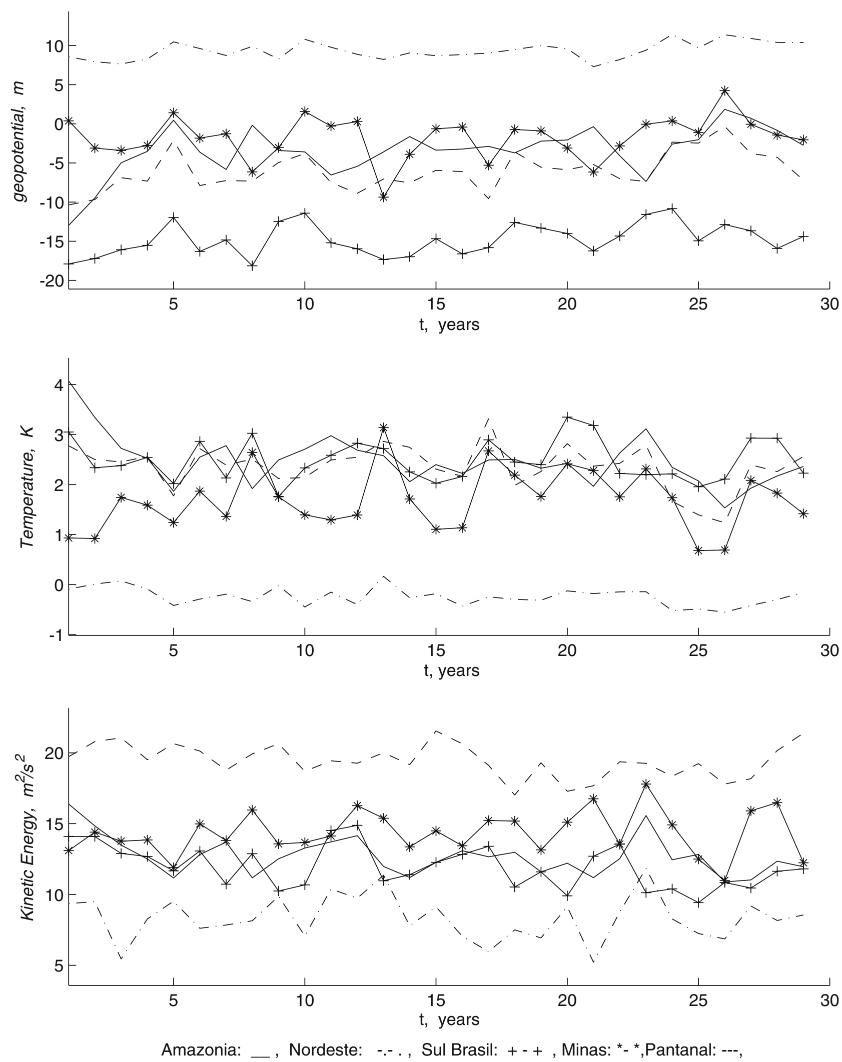

Fig. 7 Time series of mean (over the regions shown in Fig. 1) MAD, calculated for HadAM3P and ETA CCS model fields of geopotential height, G (m), temperature, T (K), and kinetic energy, KE ($m^2\ s^{-2}$) at 1,000 hPa

responsible for the discrepancies of models, even in reproducing large-scale, long-term components of circulation. We note that the values of the MAD and the amplitudes of its interannual variations for geopotential height and temperature decrease when the altitude increases (not shown). For kinetic energy, both the MAD and amplitude of interannual variations increase when the altitude increases (not shown), although the magnitude of the relative MAD (for example, normalized mean standard deviation) for kinetic energy decreases.

Figure 8 presents a scatter diagram of daily linear regression coefficient values (a0, a1) that describe the regression of the GCM 1,000 hPa geopotential height field on the same RCM field (top), the time evolution of these coefficients (middle) for each month of the model run, and the time evolution of the consistency index (bottom). The consistency index was calculated in the same way as described above (Fig. 2), but the time series were substituted for by "space" series formed by variable values at all grid points. Hypothetically, when the fields of GCM and RCM coincide, all points in the top figure should fall on one point with the coordinates a1=1.0 and a0=0.0. Thus, if the points in the top figure are located near the point (a1=1, a0=0), the compared RCM and GCM fields must be very similar, while, when the points are reasonably scattered but the center of mass of this distribution is close to the point (a1=1, a0=0), the fields of the models are similar, on average. The time series of linear regression coefficients a0 and a1 of GCM data on RCM data have a large negative correlation (middle figure). In most cases, this leads to some compensation in the variations of CI (bottom figure). The CI variations clearly express the annual oscillation. The mean value of CI is about 0.84 and increases with the altitude. Its linear time trend is very small, which indicates that the models do not diverge. Figure 9 shows the same characteristics as in Fig. 8, but for the RCM and GCM temperature fields at 1,000 hPa. The scatter diagrams in this case indicate that GCM is slightly warmer then RCM for regions with low temperatures and slightly colder for regions with higher temperatures. This

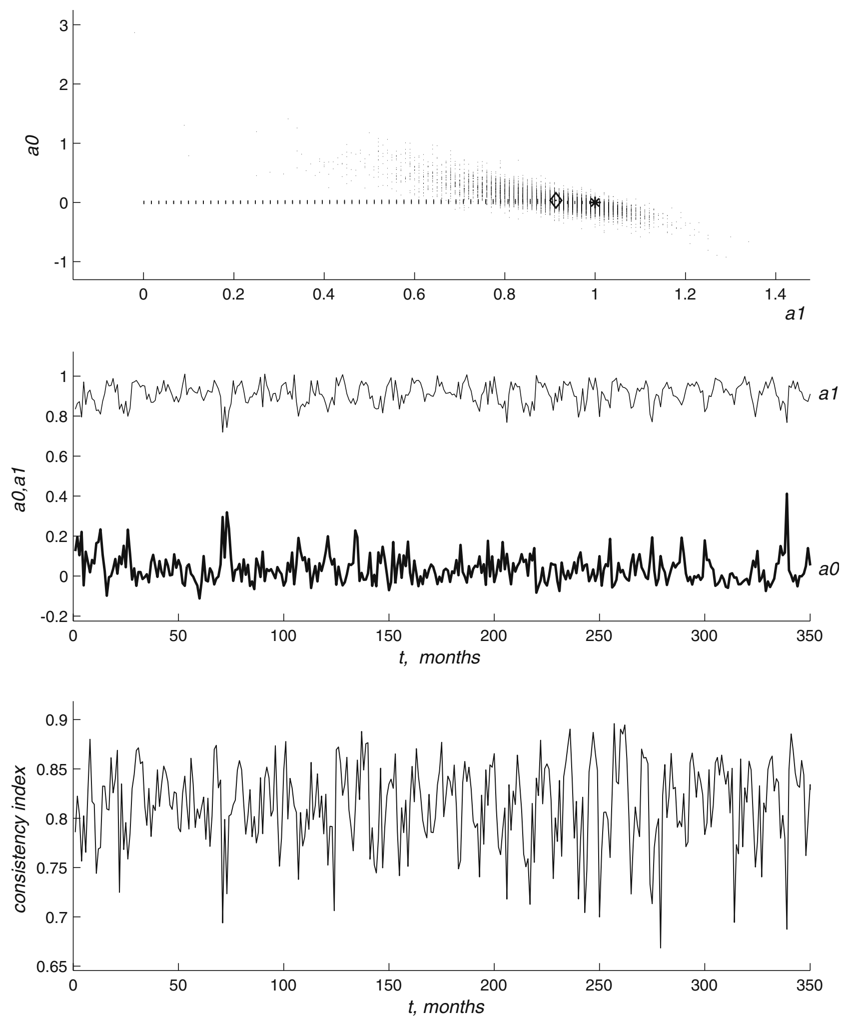

Fig. 8 Scattering diagram of daily coefficients (a0, a1) of linear regression of HadAM3P field on ETA CCS model field of geopotential height at 1,000 hPa calculated over the all integration domain (*top*); time series of regression coefficients (a0, a1) (*middle*), time series of consistency index for these models (*bottom*)

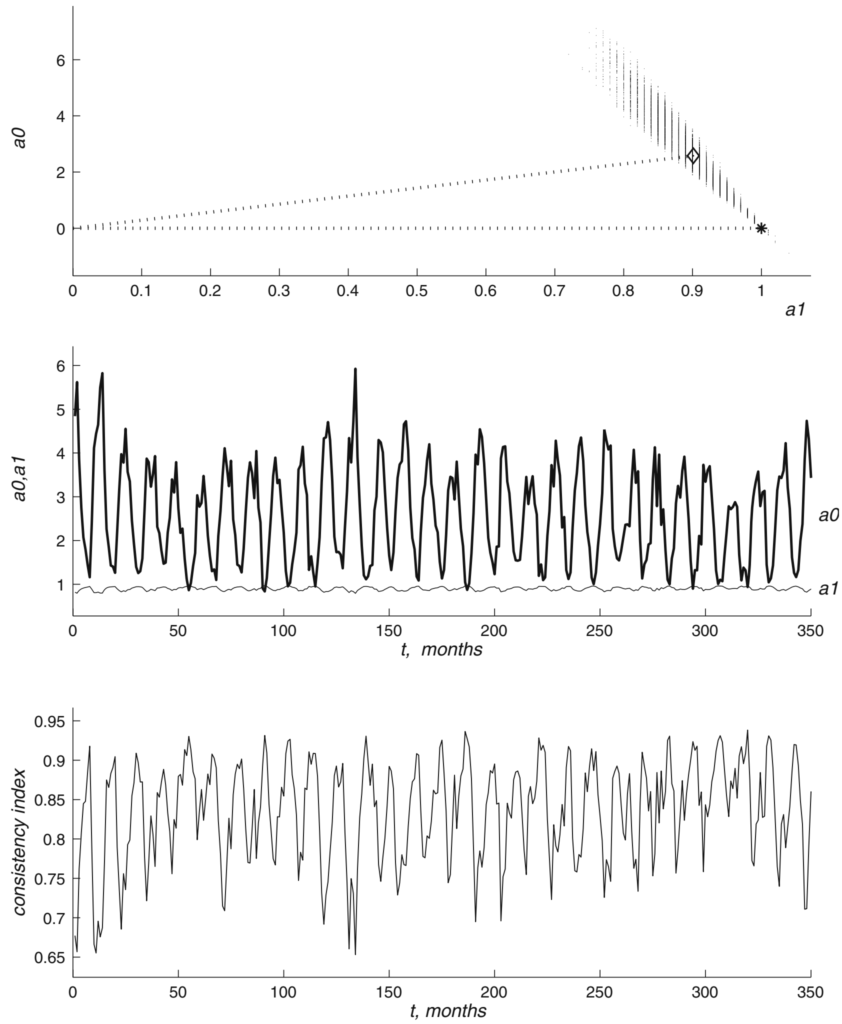

Fig. 9 The same as in Fig. 12 but for temperature at 1,000 hPa

agrees with Fig. 3, which shows mean temperature fields for the whole period of integration.

For a more detailed analysis of the time evolution of mean values of meteorological variable fields, we calculated the spectral distributions of their time series using the Fast Fourier Transform algorithm. Figure 10 shows an example of such a distribution for the time series of geopotential height, temperature, and kinetic energy averaged over the entire integration domain. It is clear that the GCM and RCM spectra have high degrees of similarity: the high frequency tails quasi coincide, the year and semi-year oscillations have the same amplitude, and the 4-year cycle in geopotential height and temperature is reproduced by RCM and GCM quasi-identically. This cycle in kinetic energy spectra is reproduced by both models, but not identically. In addition, the models both produce a 6–9 year minimum with a following increase of the spectra. Nearly all synoptic and seasonal oscillation maxima coincide in the RCM and GCM spectra. We also calculated the same spectra for the above-mentioned regions shown in Fig. 1. The RCM and GCM spectra for these regions demonstrate similar coincidences as for the whole integration domain with insignificant distinctions. Only for the Pantanal region do the spectra of GCM and RCM kinetic energy at 1,000 hPa diverge significantly. With increasing altitude, however, this difference diminishes and is nearly gone at 500 hPa (not shown). This resemblance of time spectra shows that, although the fields of investigated meteorological variables can differ because of the phase discrepancy in the compared models, the statistical behavior of their time evolution is very similar.

4 Conclusions

Our analysis of the output results of 30-year runs of the ETA regional model and its driving global model HadAM3P confirms that the models have an admissible degree of consistency despite differences in their physical parameterizations. The ETA model can reproduce the main patterns of the HadAM3P mean fields of geopotential height, temperature, and kinetic energy at various levels.

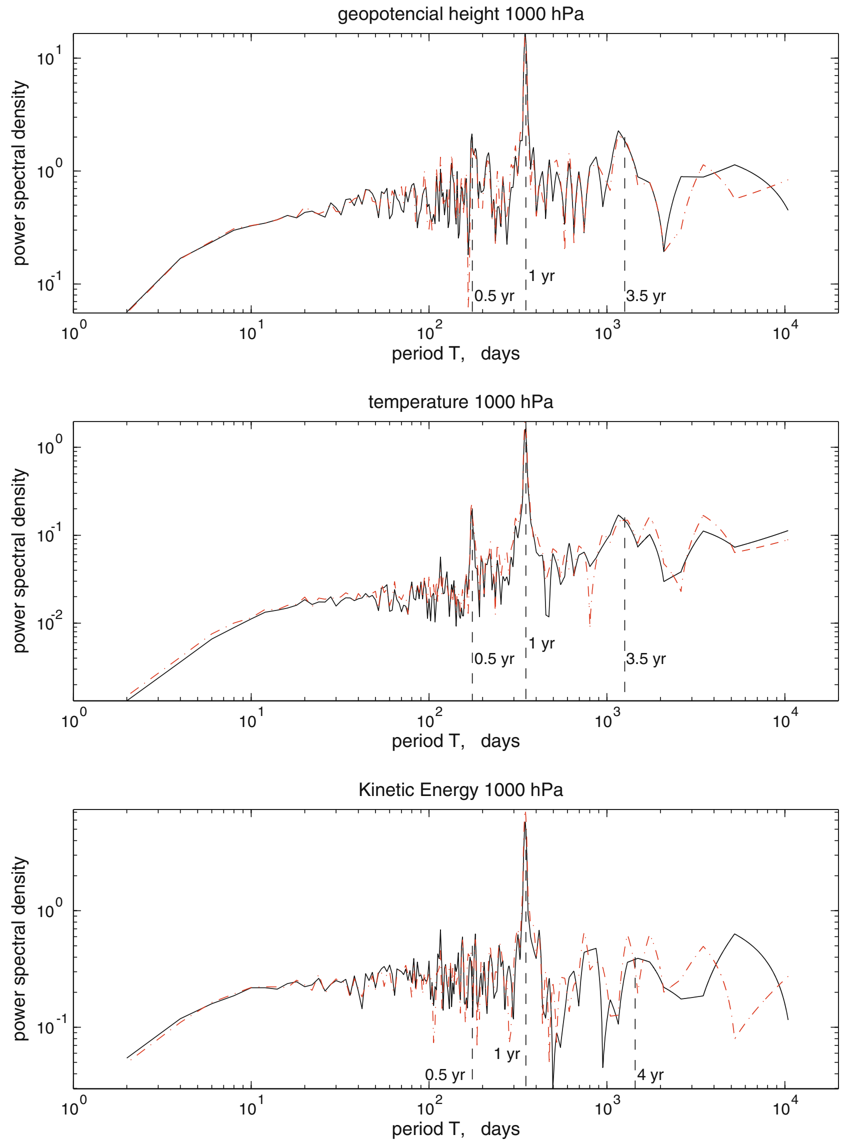

Fig. 10 Time spectra of mean (over the integration domain) geopotential height (*top*), temperature (*middle*), and kinetic energy (bottom) at 1,000 hPa, provided by HadAM3P (*solid*) and ETA CCS model (*dot-dashed*) simulations

The fields of time standard deviation of meteorological variables are also similar at all model levels. The magnitude of the mean model arithmetic difference (MAD) averaged over the domain is about 6 m in geopotential height, less than 0.1 K in temperature, and about 10 $m^2 s^{-2}$ in kinetic energy at 1,000 hPa. The low magnitude of the root mean square difference (RMSD) means that current absolute values of the MAD are not high for each moment of the integration. Notice, that the magnitude of RMSD is not larger than the usual difference between GCM and observations. There is no drift of the MAD and RMSD during the integration. The magnitude of the temporal correlation coefficient between the time series of RCM and GCM space-averaged fields is high (about 0.95–0.98), which means that the RCM follows the GCM boundary driving. The spectral analysis of the RCM and GCM fields shows that the GCM and RCM spectra have a high degree of similarity. We propose a new nondimensional consistency index for evaluating the consistency between the two models. The CI fields resemble the fields of the MAD in terms of spatial distribution, but can be used in a quantitative comparison of the similarities of the fields of different meteorological variables. The comparison of the ETA CCS and HadAM3P models shows that the new climate version of the ETA model can be used in downscaling the HadAM3P output fields.

The approach developed in this study can form the basis for quantitatively assessing the consistency of regional models and their driving global models. By applying this methodology to various RCMs located over various regions of the world, one can give useful information for the discussion about needed level of consistency between RCM and its driving GCM. Currently, many researchers use various regional models for dynamical downscaling, but

Fig. 11 DJF mean precipitation (mm day^{-1}) averaged over 1980–1983 years: **a** GPCP, **b** CRU, **c** HadAM3P, **d** ETA CCS (*bc* HadAM3P), **e** ETA CCS (bc: Reanalysis)

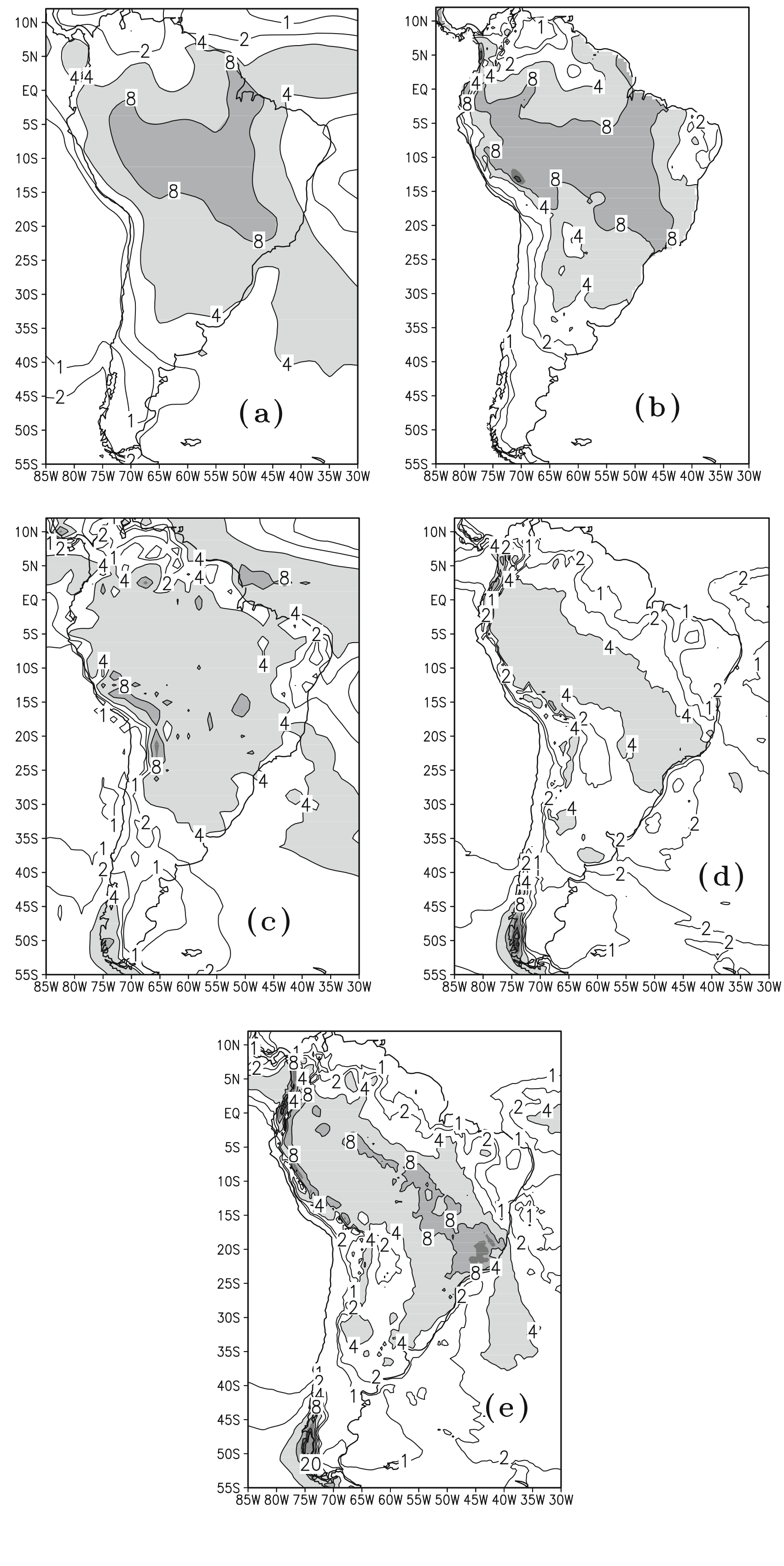

few publications quantitatively assess the similarity of the large-scale fields of a regional model and its driving global model. Even if regional and global models have the same physical parameterization packages, differences between the models may be related to the low time frequency and low space resolution of boundary forcing in the regional model. In future work, we plan to estimate the impact of tuning in RCM physical parameterizations, including radiation and convection schemes on the consistency of RCM and GCM output fields. The impact of using another driven global model on the resemblance of RCM to GCM will also be estimated.

In order to evaluate the ETA CCS model performance for the current climate, we also compared the regional model outputs with observations (Pisnichenko and Tarasova 2009). In this study, the ETA CCS model was run over South America for the period from 1979 to 1985. Two sets of boundary conditions derived from the reanalysis II (Kanamitsu et al. 2002) and from output of the HadAM3P were used for the model runs. The monthly mean output fields of model-simulated precipitation rate, precipitation frequency, and near surface air temperature were compared with the observational data of the CRU (Mitchell et al. 2004) and GPCP (Adler et al. 2003) projects. The comparison shows that the ETA model reproduces well the main patterns of observed precipitation and temperature fields in both summer and winter. The existing biases in the temperature and precipitation fields are mainly related to the deficiencies in the convection and radiation parameterization schemes of the ETA model because, in Tropics and sub-Tropics, the convection and radiation processes strongly affect the magnitude of near surface air temperature and precipitation.

The model-simulated and observed fields of mean precipitation, and near surface air temperature are shown in Figs. 11 and 12 for the austral summer months. During

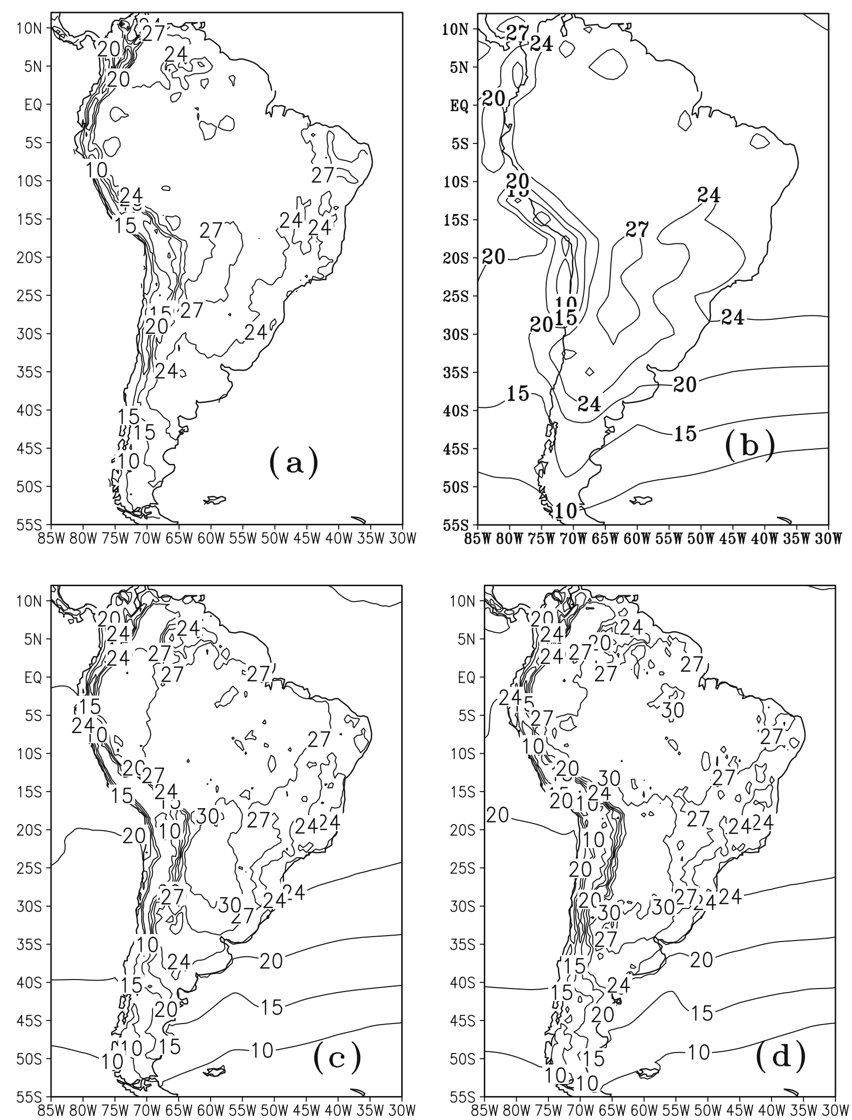

Fig. 12 DJF mean near surface air temperature (°C) averaged over 1980–1983 years: **a** CRU, **b** HadAM3P, **c** ETA CCS (*bc* HadAM3P), **d** ETA CCS (*bc* Reanalysis)

winter months, the biases are much smaller (not shown). Figure 11 shows that in summer, the HadAM3P model underestimates maximum of precipitation rate located in the central part of South Atlantic Convergence Zone. This underestimation affects the magnitude of precipitation rate simulated by the ETA model forced by HadAM3P. Figures 12 shows that the magnitude of near surface air temperature is overestimated over the central part of the continent in both ETA model runs due to the lack of convective cloudiness in this region (shown in Fig. 11).

We also studied the impact of new radiation scheme on the model-simulated precipitation averaged over the selected regions (Tarasova and Pisnichenko 2009). It was shown that during austral summer, the difference in precipitation rate caused by the change in solar radiation scheme is particularly noticeable over the regions with strong convective activity. In these regions, the difference caused by the change in boundary conditions is of the same magnitude. During winter, the modeled precipitation is affected more by the change in boundary conditions than by the change in solar radiation scheme. On the whole, these results demonstrate that the biases of the ETA CCS forced by output data of HadAM3P are not much larger than the biases of the ETA model forced by reanalysis data. Hence, further improvement of the performance of the ETA model forced by various sets of boundary conditions over South America can be achieved by improving the physics parameterization package of the ETA model.

Acknowledgements I.A. Pisnichenko was supported by Global Opportunity Fund (GOF) from UK Foreign Commonwealth Office, T.A. Tarasova was sponsored by INPE/CPTEC as part of an international agreement with the NEC Corporation. The authors thank Hadley Center for presenting HadAM3P data. We also acknowledge Prof. R. Laprise for useful discussion during preparing manuscript.

Appendix 1. Recurrence formulas

For the evaluation of the consistency of the models we analyzed very large series of the meteorological data. To make the work with series faster and for economy of computer resources, we used recurrence formulas for calculating running average, SD, and covariance, from which we can calculate any other necessary characteristics. Unfortunately, these formulae are not easy to find. We encounter recurrence formula for SD only in one programming book (Knuth 1997).

We accept the definition of running mean, variance, and covariance, respectively, as

$$\overline{x}_n = \frac{1}{n}\sum_{i=1}^{n} x_i, \tag{4}$$

$$D_n = \frac{1}{n}\sum_{i=1}^{n}(x_i - x_n)^2, \tag{5}$$

$$r_n = \frac{1}{n}\sum_{i=1}^{n}(x_i - \overline{x}_n)(y_i - \overline{y}_n). \tag{6}$$

Here, x_n, D_n, and r_n are the sample mean, the sample variance, and the sample covariance for serieses containing n terms, x_i, y_i, are the i-th term of series. The recurrence formula for a sample mean is obvious

$$\overline{x}_n = \frac{n-1}{n}x_{n-1} + \frac{1}{n}x_n. \tag{7}$$

Below, we derive the recurrence formula for a sample covariance. The analogous formula for a sample variance is obtained after replacing y_i, $\overline{y}_n$ by x_i, $\overline{x}_n$.

Let us rewrite formula 6 using Eq. 7 in following manner

$$r_n = \tfrac{n-1}{n}\cdot\tfrac{1}{n-1}\sum_{i=1}^{n-1}\left(x_i - \tfrac{n-1}{n}\overline{x}_{n-1} - \tfrac{1}{n}x_n\right)\left(y_i - \tfrac{n-1}{n}\overline{y}_{n-1} - \tfrac{1}{n}y_n\right) + \\ + \tfrac{1}{n}(x_n - \overline{x}_n)(y_n - \overline{y}_n)$$

Now, we group the members of this formula to select the part that is equal to the covariance on previous $(n-1)$ step

$$\begin{aligned} r_n = {} & \tfrac{n-1}{n}\cdot\tfrac{1}{n-1}\sum_{i=1}^{n-1}(x_i - \overline{x}_{n-1})(y_i - \overline{y}_{n-1}) \\ & + \tfrac{1}{n}(\overline{y}_{n-1} - y_n)\cdot\tfrac{n-1}{n}\cdot\tfrac{1}{n-1}\sum_{i=1}^{n-1}(x_i - -\overline{x}_{n-1}) \\ & + \tfrac{1}{n}(\overline{x}_{n-1} - x_n)\tfrac{n-1}{n}\cdot\tfrac{1}{n-1}\sum_{i=1}^{n-1}(y_i - \overline{y}_{n-1}) \\ & + \tfrac{1}{n}(\overline{x}_{n-1} - x_n)\cdot\tfrac{1}{n}(\overline{y}_{n-1} - y_n)\cdot\tfrac{n-1}{n} \\ & + \tfrac{1}{n}(x_n - \overline{x}_n)(y_n - \overline{y}_n). \end{aligned}$$

Taking into account that the terms $\frac{1}{n-1}\sum_{i=1}^{n-1}(x_i - x_{n-1})$ and $\frac{1}{n-1}\sum_{i=1}^{n-1}(y_i - \overline{y}_{n-1})$ are equal to zero and using again formula 7, we obtain

$$r_n = \frac{n-1}{n}r_{n-1} + \frac{n-1}{n^2}(\overline{x}_{n-1} - x_n)(\overline{y}_{n-1} - y_n). \tag{8}$$

Finally, we show how to recalculate these running values for any time interval. Let x_m be the mean value for series from the first m elements of x_i and let $m<n$. Denote $x_{m:n}$ the mean value of x_i for the series x_{m+1}, x_{m+2}, x_n as

$$\overline{x}_{m:n} = \frac{1}{n-m}\sum_{i=m+1}^{n} x_i,$$

It is easy to obtain that

$$\overline{x}_{m:n} = \frac{1}{n-m}(n\overline{x}_n - m\overline{x}_m). \tag{9}$$

Now, let us derive the formula for calculating the covariance for interval (m+1,n) using the meanings for covariance and average for intervals (1,m) and (1,n).

$$n\overline{r}_n - m\overline{r}_m = \sum_{i=1}^{n}(x_iy_i) - n\overline{x}_n\overline{y}_n - \sum_{i=1}^{m}(x_iy_i) + m\overline{x}_m\overline{y}_m \quad (10)$$

Taking into account that

$$(n-m)\overline{r}_{m:n} = \sum_{i=m+1}^{n}(x_iy_i) - (n-m)\overline{x}_{m:n}\overline{y}_{m:n}, \quad (11)$$

we rewrite Eq. (10) as

$$n\overline{r}_n - m\overline{r}_m = (n-m)\overline{r}_{m:n} - n\overline{x}_n\overline{y}_n + m\overline{x}_m\overline{y}_m + (n-m)\overline{x}_{m:n}\overline{y}_{m:n}. \quad (12)$$

Lastly, substituting the $x_{m:n}, y_{m:n}$ from formula 9 and making routine transformations, we obtain the desired formula

$$\overline{r}_{m:n} = \frac{1}{n-m}(n\overline{r}_n - m\overline{r}_m) - \frac{mn}{(n-m)^2}(\overline{x}_n - \overline{x}_m)(\overline{y}_n - \overline{y}_m). \quad (13)$$

References

Adler RF et al (2003) The version 2 Global Precipitation Climatology Project (GPCP) monthly precipitation analysis (1979–present). J Hydrometeor 4:1147–1167

Betts AK, Miller MT (1986) A new convective adjustment scheme. Part II: Single column tests GATE wave, BOMEX, and Arctic air-mass data. Quart J Roy Met Soc 112:693–703

Black TL (1994) NMC notes: the new NMC mesoscale Eta model: description and forecast examples. Wea Forecasting 9:256–278

Castro CL, Pielke Sr RA, Leoncini G (2005) Dynamical downscaling: Assessment of value retained and adding using the Regional Atmospheric Modeling System (RAMS). J Geophys Res 110 (D05108) doi:10.1029/2004JD004721

Chen FK, Janjic Z, Mitchel K (1997) Impact of the atmospheric surface-layer parameterizations in the new land-surface scheme of the NCEP mesoscale Eta model. Bound-Layer Meteor 85:391–421

Chou M-D, Suarez MJ (1999) A solar radiation parameterization (CLIRAD-SW) for atmospheric studies. Preprint NASA/Goddard Space Flight Center, Greenbelt, Maryland, p 38

Chou SC, Nunes AMB, Cavalcanti IFA (2000) Extended forecast over South America using the regional Eta model. J Geophys Res 105:10147–10160

Chou M-D, Suarez MJ, Liang X-Z, M-H YM (2001) A thermal infrared radiation parameterization for atmospheric Studies. Preprint NASA/Goddard Space Flight Center, Greenbelt, Maryland, p 55

Christensen JH, Carter TR, Rummukainen M, Amanatidis G (2007) Evaluating the performance and utility of regional climate models: The PRUDENCE project. Climatic Change 81:1–6

Dickinson RE, Errico RM, Giorgi F, Bates GT (1989) A regional climate model for the western United States. Clim Change 15:383–422

Duffy PB, Arritt RW, Coquard J, Gutowski W, Han J, Iorio J, Kim J, Leung L-R, Roads J, Zeledon E (2006) Simulations of present and future climates in the western United States with four nested regional climate models. J Clim 19:873–895

Fels SB, Schwartzkopf MD (1975) The simplified exchange approximation: a new method for radiative transfer calculations. J Atmos Sci 32:1475–1466

Fernandez JPR, Franchito SH, Rao VB (2006) Simulation of the summer circulation over South America by two regional climate models. Part I: Mean climatology. Theor Appl Climatol 86:247–260

Giorgi F, Bates GT (1989) The climatological skill of a regional model over complex terrain. Mon Wea Rev 117:2325–2347

Giorgi F, Bi X, Pal JS (2004) Mean, interannual variability and trends in a regional climate change experiment over Europe. I. Present-day climate (1961–1990). Clim Dyn 22:733–756. doi:10.1007/s00382-004-0409-x

Hong S-Y, Yuang H-M, Zhao Q (1998) Implementing of prognostic cloud scheme for a regional spectral model. Mon Wea Rev 126:2621–2639

Hudson DA, Jones RD (2002) Regional climate model simulations of present-day and future climates of Southern Africa. Hadley Centre for Climate Prediction and Research, Met Office, Bracknell, UK

Janjic ZI (1994) The step-mountain eta coordinate model: further development of the convection, viscous sublayer, and turbulence closure schemes. Mon Wea Rev 122:927–945

Jones RG, Murphy JM, Noguer M, Keen AB (1997) Simulation of climate change over Europe using a nested regional-climate model. II: Comparison of driving and regional model responses to a doubling of carbon dioxide. Quart J Roy Met Soc 123:265–292

Jones RG, Noguer M, Hassel DC, Hudson D, Wilson SS, Jenkins GJ, Mitchell JFB (2004) Generating high resolution climate change scenarios using PRECIS. Met Office, Hadley Center, Exeter, UK, p 40

Kain JS, Fritsch JM (1993) A one-dimensional entraining detraining plume model and its applications in convective parameterization. J Atmos Sci 23:2784–2802

Kanamitsu M, Ebisuzaki W, Woollen J, Yang S-K, Hnilo JJ, Fiorino M, Potter GL (2002) NCEP-DOE AMIP-II Reanalysis (R-2). Bull Amer Meteor Soc 83:1631–1643

Knuth DE (1997) The art of computer programming, vol. 2: Seminumerical algorithms, 3rd edn. Addison-Wesley, Reading, Massachusetts, p xiv+762 ISBN 0-201-89684-2

Lacis AA, Hansen JE (1974) A parameterization for the absorption of solar radiation in the Earth's atmosphere. J Atmos Sci 31:118–133

Laprise R (2006) Regional climate modelling. J Comput Phys. doi:10.1016/j.jcp.2006.10.024

Laprise R, Caya D, Frigon A, Paquin D (2003) Current and perturbed climate as simulated by the second-generation Canadian Regional Climate Model (CRCM-II) over north-western North America. Clim Dyn 21:405–421. doi:10.1007/s00382-003-0342-4

Laprise R, de Elia R, Caya D, Biner S, Lucas-Picher P, Diaconescu E, Leduc M, Alexandru A, Separovic L, Canadian Network for Regional Climate Modelling and Diagnostics (2008) Challenging some tenets of regional climate modelling. Meteorol Atmos Physic 100:3–22. doi:10.1007/s00703-008-0292-9

Mellor GL, Yamada T (1974) A hierarchy of turbulence closure models for boundary layers. J Atmos Sci 31:1791–1806

Mesinger F, Janjic ZI, Nickovic S, Gavrilov D, Deaven DG (1988) The step-mountain coordinate: model description and performance for cases of Alpine lee cyclogenesis and for a case of Appalachian redevelopment. Mon Wea Rev 116:1493–1518

Mitchell TD, Carter TR, Jones PD, Hulme M, New M (2004) A comprehensive set of high-resolution grids of monthly climate for Europe and the globe: the observed record (1901–2000) and 16 scenarios (2001–2100). Working paper 55. Tyne Center for Climate Change Research, University of East Anglia, Norwich, UK, p 30

Pielke RA Sr et al (1992) A comprehensive meteorological modeling system—RAMS. Meteorol Atmos Phys 49:69–91

Pisnichenko IA, Tarasova TA (2009) The climate version of the Eta regional forecast model. II. Evaluation of the Eta CCS model performance against reanalysis data and surface observations. arXiv:0901.1461v1 [physics.ao-ph] (http://arxiv.org/abs/0901.1461v1)

Pisnichenko IA, Tarasova TA, Fernandez JPR, Marengo J (2006) Validation of the Eta WS regional climate model driven by boundary conditions from the HADAM3P over South America. Proceedings of 8 ICSHMO, Foz do Iguacu, Brazil, April 24–28, INPE, pp 595–597

Pisnitchenko FI, Pisnichenko IA, Martinez JM, Santos SA (2008) Continuing dynamic assimilation of the inner region data in hydrodynamics modelling: optimization approach. Nonlin Processes Geophys 15:815–829

Seth A, Rauscher SA, Camargo SJ (2007) RegCM3 regional climatologies for South America using reanalysis and ECHAM global model driving fields. Clim Dyn 28:461–480. doi:10.1007/s00382-006-0191-z

Slingo JM (1987) The development of a cloud prediction model for the ECMWF model. Quart J Royal Met Soc 113:899–927

Tarasova TA, Fomin BA (2000) Solar radiation absorption due to water vapor: advanced broadband parameterizations. J Appl Meteor 39:1947–1951

Tarasova TA, Pisnichenko IA (2009) Performance of various radiation parameterizations in the climate version of the Eta regional model driven by reanalysis and HadAM3P. in: Proceedings IRS2008: Current Problems in Atmospheric Radiation

Tarasova TA, Fernandez JPR, Pisnichenko IA, Marengo JA, Ceballos JC, Bottino MJ (2006) Impact of new solar radiation parameterization in the Eta Model on the simulation of summer climate over South America. J Appl Meteor Climatol 44:318–333

Taylor KE (2001) Summarizing multiple aspects of model performance in single diagram. J Geophys Res 106:7183–7192

Wang Y, Leung LR, McGregor JL, Lee D-K, Wang W-C, Ding Y, Kimura F (2004) Regional climate modeling: progress, challenges, and prospects. J Meteor Soc Jpn 82:1599–1628

Xu K-M, Randall DA (1996) A semi empirical cloudiness parameterization for use in climate models. J Atmos Sci 53:3084–3102